Electronic Supplementary Material (ESI) for Nanoscale.

Supporting information

Restoring self-limited growth of single-layer graphene on copper foil *via* backside coating

Nicolas Reckinger, Marcello Casa, Jeroen E. Scheerder, Wout Keijers, Matthieu Paillet, Jean-Roch Huntzinger, Emile Haye, Alexandre Felten, Joris Van de Vondel, Maria Sarno, Luc Henrard, and Jean-François Colomer

Table of contents

1) Reproducibility issues

As-received copper foils must be processed before graphene growth. Notably, they are often covered with thin metallic oxide anticorrosion coatings.[1,2,3] Several groups also have reported the presence of particles of endogenous origin (copper particles formed during hydrogen annealing at elevated temperature[4,5] or resulting from the reduction of copper oxide particles formed during annealing without hydrogen,[6,7] impurities arising from segregation from the bulk of the copper foil,[8,9] or already present on the as-received surface[7,10,11,12] (see Table S1 for reported compositions)) or exogenous origin (contaminants from the quartz tube[13,14,15,16] or back streaming from downstream system components[17]). These particles promote few-layer graphene (FLG) nucleation,[4,10,12] prevent full-coverage graphene growth[12] or cause the etching of graphene.[16]

Reference	Elements detected	Copper foil	Detection method
[2]	Ca, P, Cr	Alfa Aesar #13382	XPS
	Si	Alfa Aesar #10950	XPS
	Si	Alfa Aesar #42972	XPS
[7]	Ca, P, Cr, N, Cl, O	Alfa Aesar #13382	XPS
[10]	Si, Ca, Pt, Ru, Ce	Alfa Aesar (25 µm, 99.8% purity)	EDX
[12]	Si, Fe, Al, Ca, C, O	Not mentioned	EDX

Table S1: Composition of impurities located on as-received copper foils reported in the literature.

A) Cleaning of the copper samples

We investigate here the cleaning of the copper foils to remove the impurity particles and/or the coating. Many different pretreatment techniques have been proposed such as: (1) chemical treatment in various liquids such as acetic acid,[2,18,19,20,21,22,23] solvents,[24] water,[18,25] inorganic acids (dilute HNO_3,[11,18] dilute HCl[11,26,27]), $FeCl_3$,[6,18] Cr or Ni etchants;[11] (2) electropolishing (EP)[3,18,19,20] and (3) chemical mechanical polishing.[4] More particularly, the popular removal of superficial copper oxide with acetic acid was shown to be very effective.[28] In the perspective of large-scale production, it also presents the distinctive asset not to involve complicated treatments or hazardous chemicals. Finally, some research groups even produced their own copper foils to have a tighter control on purity and roughness.[17,29]

We analyze the surface composition of as-received copper substrates by X-ray photoelectron spectroscopy (XPS) to assess the presence of contaminants. Two as-received samples (1×1 cm^2) from two different AA #46365 30×30 cm^2 batches are analyzed at three distinct randomly chosen spots. The concentration of the detected elements is determined from the survey scan (see Figure S1a). Besides copper, the main detected elements are oxygen (O 1*s*) and carbon (C 1*s*), corresponding to organic contamination. Chromium (Cr 2*p;* ~2%) is also unambiguously identified on both copper foils. Surprisingly, it indicates the presence of a layer of chromium oxide (the anticorrosion coating mentioned above), even though the AA #46365 copper foils are supposed to be coating-free (see Figure S1b displaying the high-resolution Cr core level spectra of three copper samples: as-received, reference (pure copper ingot), after growth). Other peaks are attributed to calcium (Ca 2*p*; ~6%) and phosphorus (P 2*p*; ~7%). The concentrations in the different elements can be found in Table S2. Besides it is worth noting that Murdock *et al.* have identified that the surface composition can vary from point to point on the same 30×30 cm^2 copper foil.[10] In our previous work,[7] we have relied on a cleaning mixture composed of glacial acetic acid (GAA) and deionized water (DIW) to remove the calcium- and phosphorus-bearing impurities. Figure S1c evidences the complete absence of graphene after growth in the *standard* conditions (*i.e.* a dilute CH_4 flow of 0.5 sccm and a growth duration of 1 h) on an as-received sample inspected by scanning electron microscopy (SEM). All the W-free samples presented here are grown in these conditions. The inset to Figure S1c shows the corresponding C 1*s* core level spectrum compared to the typical C 1*s* core level spectrum of single-layer graphene grown by chemical vapor deposition (CVD) (cleaning performed in GAA+DIW). Still, this GAA+DIW treatment does not strip the chromium oxide layer. Therefore, it is irrelevant to remove the superficial copper oxide layer, even though GAA is widely used for that purpose in the literature on coated copper foils (like the mainstream AA 13382 foils). However, even though the chromium oxide layer is not removed after the GAA+DIW treatment, it is evaporated during the pre-growth annealing.[7] In conclusion, the analysis of the composition of the copper foil after graphene growth indeed confirms that, within the detection limit of XPS, the contamination layers are removed (see Figure S1a).

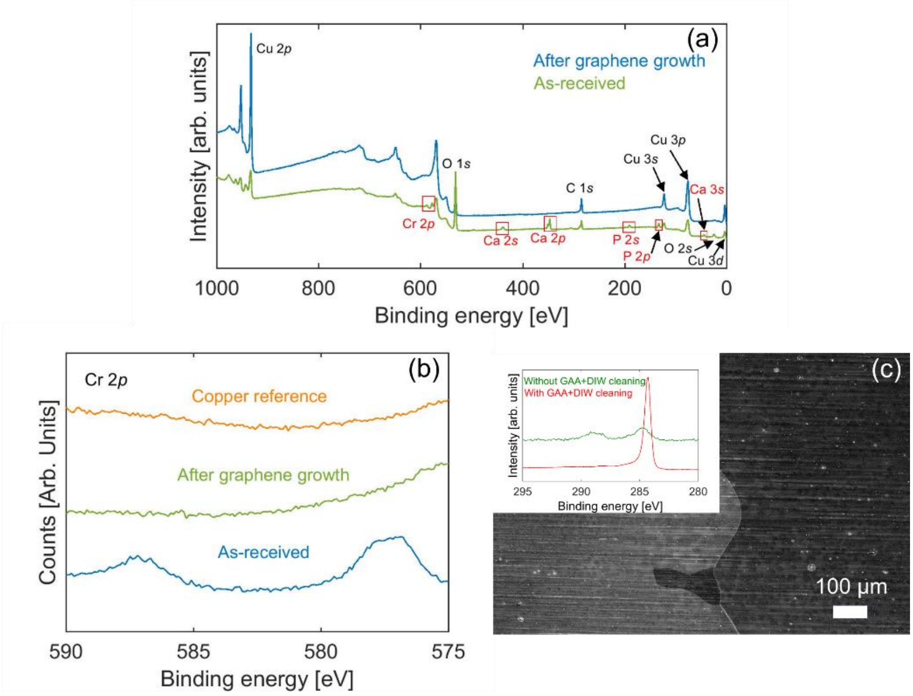

Figure S1: (a) X-ray photoelectron spectroscopy survey scan of the as-received and the graphene/copper samples. (b) Cr 2*p* core level spectra for the as-received, the graphene/copper, and the reference (pure copper ingot) copper pieces, respectively. (c) Scanning electron microscopy image of a post-growth copper piece without any pre-growth treatment displaying two large copper grains. Inset: C 1*s* core level spectra of two post-growth copper piece: one cleaned in the mixture of glacial acetic acid and deionized water and the other one without any pre-growth cleaning.

Despite this efficient treatment, the large-scale inspection of more than 25 1×1 cm^2 graphene/copper pieces coming from all over the surface of the 30×30 cm^2 batch by low-magnification SEM of graphene grown under the standard conditions manifests poor reproducibility both in terms of coverage and FLG formation (see Figure S2a,b and Figure S3a-c). Only 50% of the samples are fully covered, with a highly variable amount of FLG. One could naively argue that higher coverage can be reached by increasing the dilute methane flow, but this is done at the expense of the FLG concentration. In the following text, we only provide data for a few representative samples.

		Atomic composition [%]					
Sample type	Point	O 1*s*	Cu 2*p*	C 1*s*	Ca 2*p*	P 2*p*	Cr 2*p*
As- received batch #1	1	51.34	11.79	23.82	5.28	6.02	1.75
	2	50.36	11.33	25.02	5.27	6.46	1.56
	3	50.95	11.54	24.04	5.36	6.33	1.78
As- received batch #2	1	54.3	12.44	17.73	6.21	7.18	2.14
	2	53.26	12.22	19.8	6.03	6.71	1.98
	3	54.1	10.57	19.22	6.5	7.24	2.36
After graphene growth	1	23.04	43.42	34.54	X	X	X
	2	24.62	41.75	33.63	X	X	X
	3	23.09	47.38	29.53	X	X	X

Table S2: Surface composition, obtained from X-ray photoelectron spectroscopy analyses, of two as-received Alfa Aesar #46365 copper samples from two different batches, and one sample after graphene growth under the standard conditions.

A first cause for this lack of reproducibility and homogeneity is the incomplete surface contamination removal. Upon closer inspection by SEM (see Figure S2d), we can indeed observe that micro- and nanoparticles still reside on the copper foil after graphene growth. Note that XPS is not sensitive enough to detect them. All these particles (present on the copper foil at the same location before the CVD growth) cause discontinuities in the graphene film because they hinder graphene growth at their location (see Figure S2c and Figure S3a), and in addition some of them are the source of uncontrolled FLG island nucleation (see Figure S2d). For instance, as observed in Figure S2c, the graphene coverage on this copper piece is almost complete except for a small uncovered area. By zooming on this area (see Figure S2d), we can observe that it is covered by a line of particles of various sizes. Energy-dispersive X-ray spectroscopy can be used for a targeted analysis of these particles but it must be conducted on large enough (micron-sized) particles since prohibitively high acquisitions times are necessary to resolve nanometer-sized particles. The composition of two randomly selected areas in the graphene-free zone reveals the presence of aluminum oxide, silicon oxide, and carbon, as already reported in Ref. [10] (see Figure S4 and Table S3 for the precise composition).

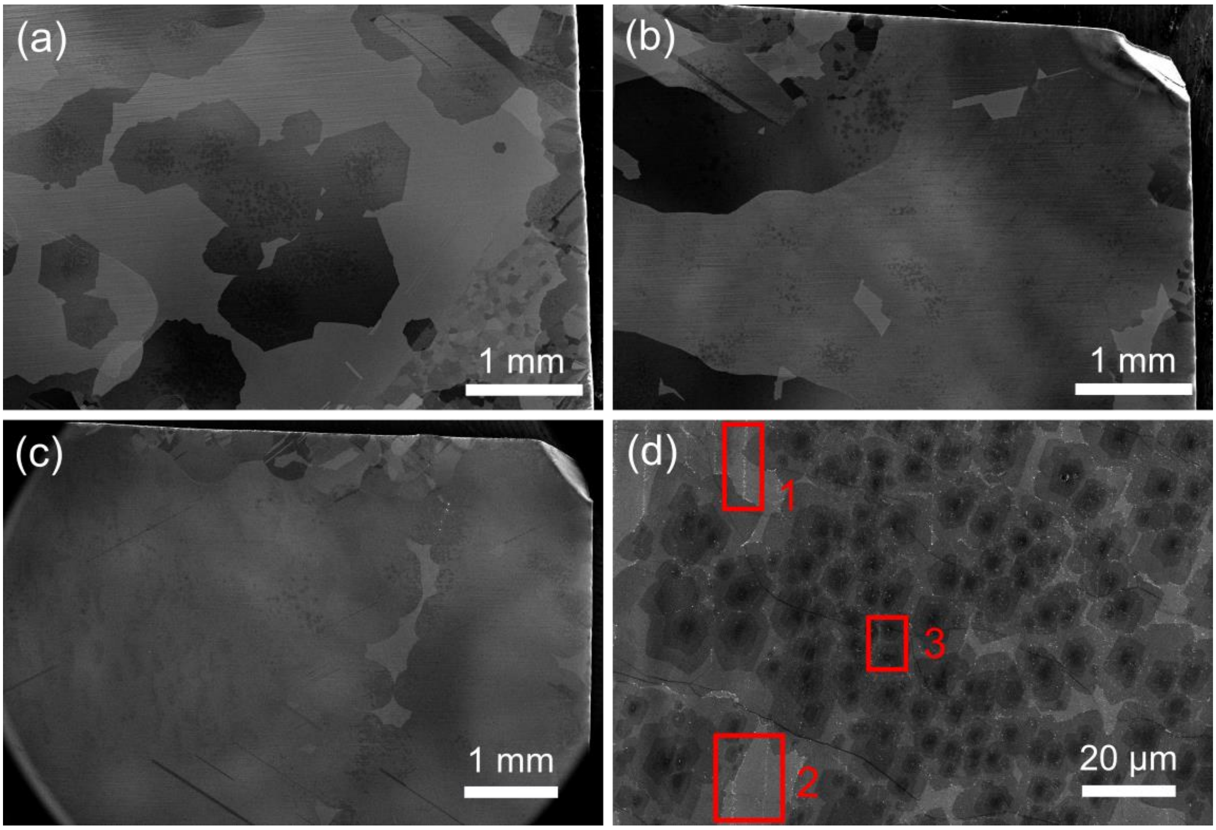

Figure S2: (a-c) Low-magnification scanning electron microscopy picture of two samples grown sequentially in the standard conditions. (d) Zoom-in on an area with a high-density of few-layer graphene islands. The red rectangles 1 and 2 illustrate the presence of white particles along the rolling striations and the rectangle 3 the nucleation of few-layer graphene on white particles.

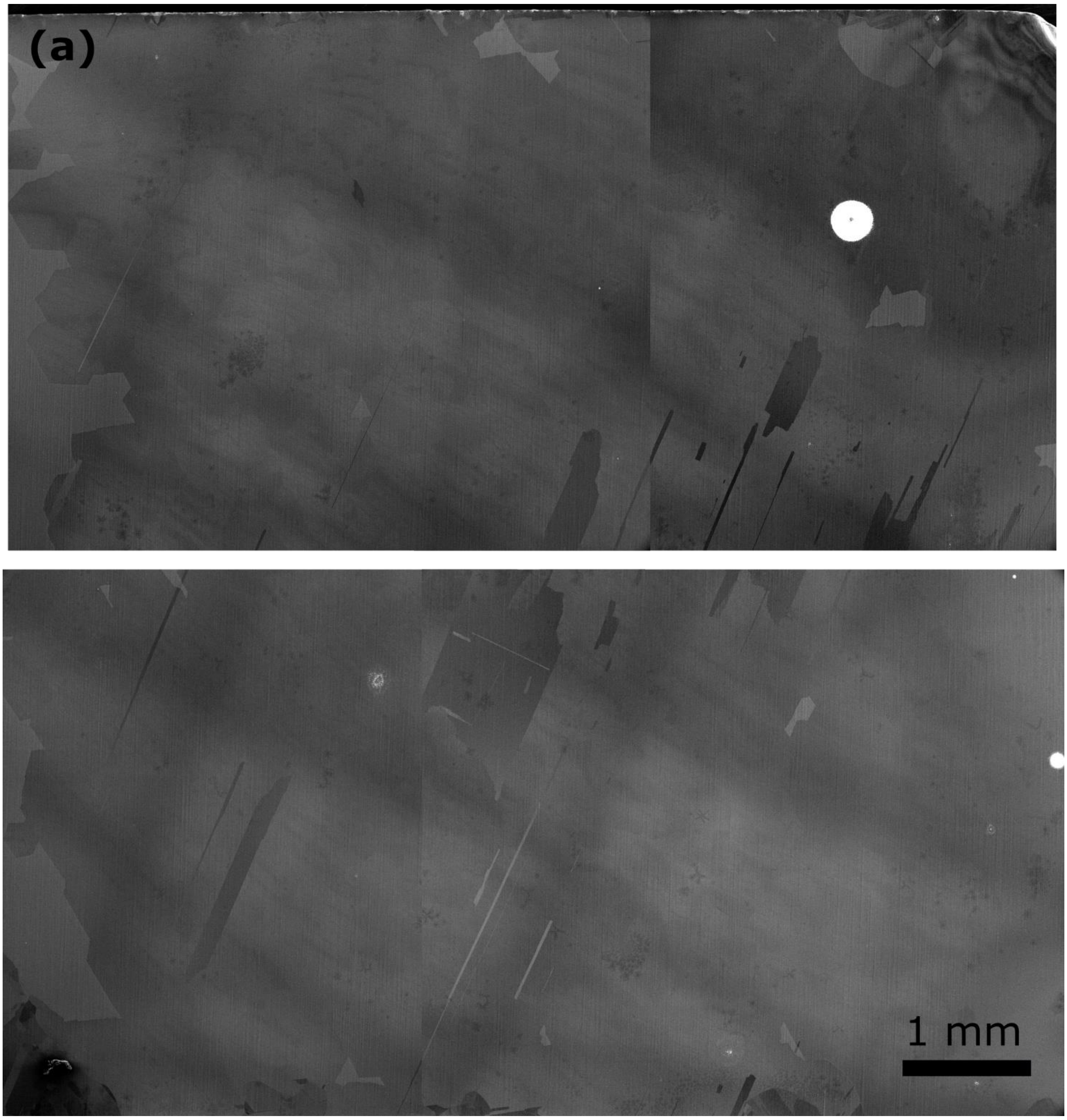
(a)
1 mm

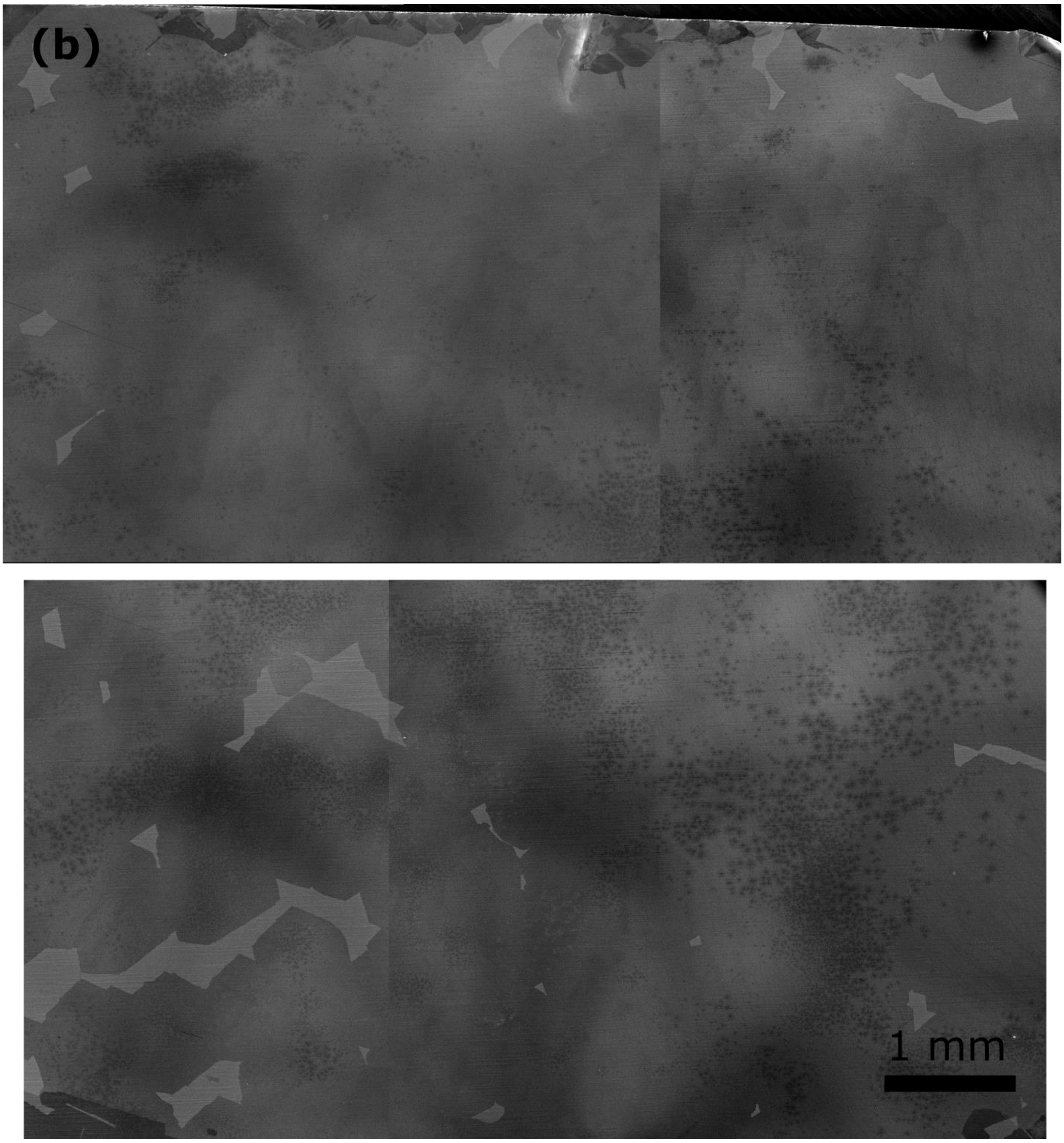
(b)
1 mm

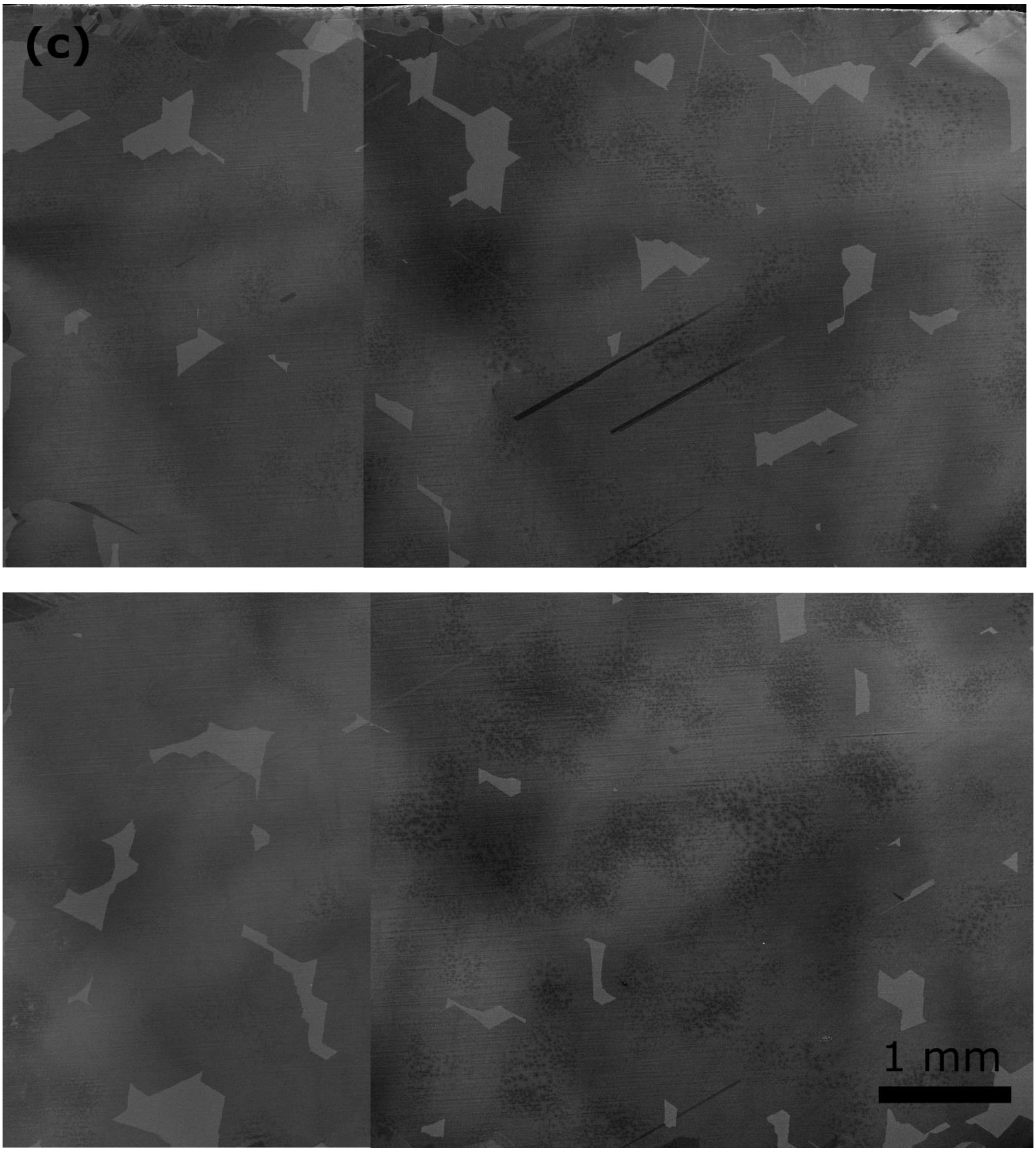

Figure S3: (a)-(c) Low-magnification scanning electron microscopy pictures of the whole surface of three samples grown altogether in the standard conditions. The bottom and top halves in each figure are formed by stitching two pictures together.

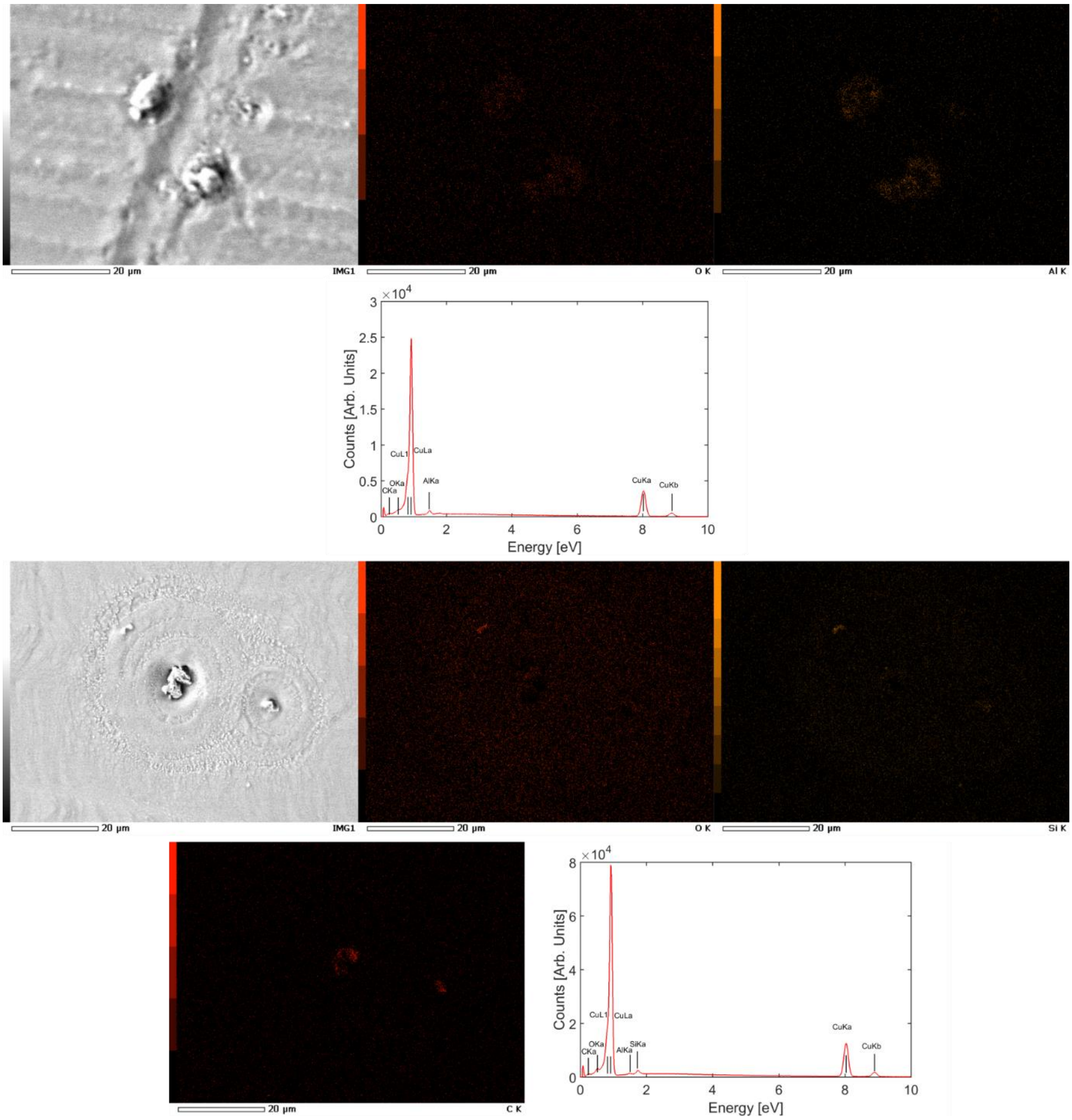

Figure S4: Energy-dispersive X-ray spectroscopy elemental mappings and spectra of two graphene-free areas for a graphene/copper sample grown under the standard conditions, exhibiting micrometer-sized particles.

Atomic composition [%]					
Area	C K	O K	Al K	Si K	Cu K
1	10.34	2.49	2.93	X	84.24
2	9.64	4.29	0.6	1.46	84.02

Table S3: Elemental composition of the two areas investigated in Figure S4.

In order to reduce the presence of these particles, we test various other chemical cleanings/etchings found in the literature, with chemicals such as (1) dilute nitric acid (5% in water), (2) hydrochloric acid dip followed by potassium hydroxide dip, with an intermediate rinsing in DIW (same conditions as in Ref. [10]), (3) ammonium persulfate (0.3 M), (4) GAA+DIW followed by immersion in Transene chromium etchant. Unfortunately, in our conditions, none of these methods give satisfactory results to jointly realize uniformity and repeatable coverage of graphene (see Figure S5). For surface copper etching, the treatments increase the roughness,[11] providing more defective regions prone to nanoparticle formation during the oxidative pre-growth annealing (see just below).

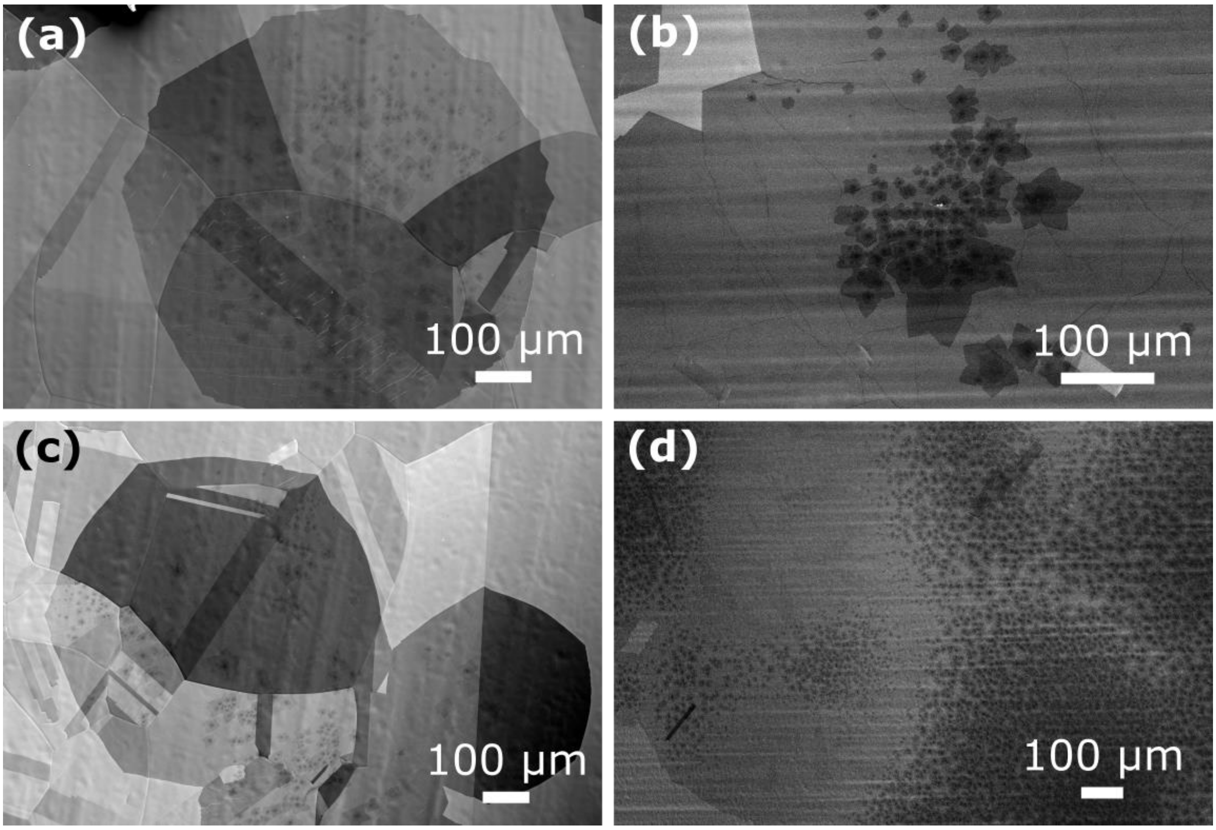

Figure S5: Scanning electron microscopy images of several samples grown under the standard conditions, subjected to diverse pre-growth chemical treatments: (a) dilute nitric acid, (b) hydrochloric acid dip followed by potassium hydroxide dip, with an intermediate rinsing in deionized water (c) ammonium persulfate, (d) mixture of glacial acetic acid and deionized water followed by immersion in Transene chromium etchant. None of these techniques lead to reproducibility in terms of coverage and homogeneity simultaneously. It is however worth mentioning that treatment (b) results in full graphene coverage, but with areas comprising few-layer graphene islands.

B) Electropolishing of the copper samples

We now turn our attention to a more radical treatment: EP (see the experimental section of the main manuscript for more details). EP is an appealing preparation technique since it implies the removal of Cu atoms from the surface of the foil together with the contaminants. In Figure S6a-b, we show the same copper stripe (2×8 cm^2) before and after EP. The reproducibility of the technique in terms of graphene coverage is assessed by growing graphene (still in the standard conditions) on nine ~1×1 cm^2 copper pieces cut from three different EP batches. Figure S6c displays a photograph of the nine copper pieces after growth and oxidation at 150 °C for 5 min on a heating plate to reveal bare copper. It appears clearly that the EP process leads to very reproducible graphene coverage since the copper foil is not oxidized (reddening of the surface). The improvement in coverage control obtained for 9 samples synthesized in a row from different EP batches is an indication that EP, as expected, removes all the surface contamination on the copper specimens. However, it is not yet completely satisfying as far as uniformity is concerned, as exemplified by the picture shown in Figure S6d. We believe that this may be due to the poor control over the amount of residual gaseous oxidizing impurities during the hydrogen-free pre-growth annealing, inducing the formation of Cu oxide nanoparticles then transformed into Cu nanoparticles after reduction under hydrogen (see Figures S7 and 8 below). We investigate that further in the next subsection C.

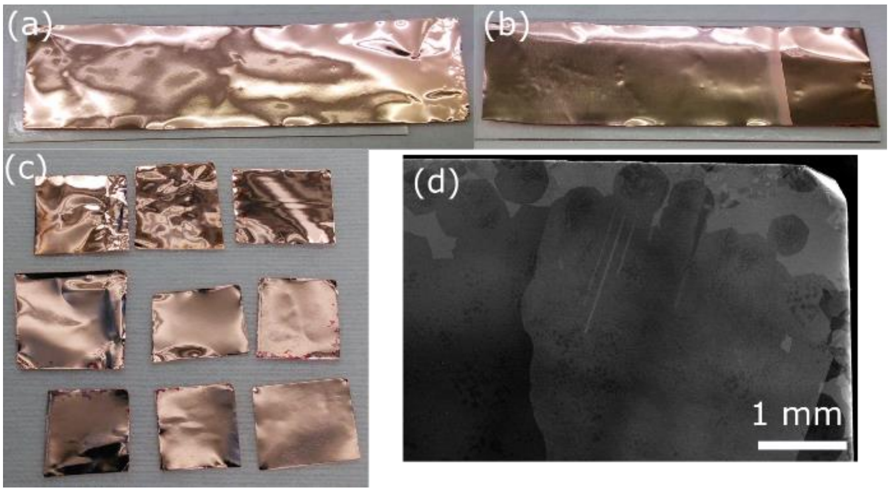

Figure S6: Photographs of the same copper stripe (a) before and (b) after electropolishing. (c) Photograph of nine electropolished copper specimens after graphene growth in the standard conditions. (d) Low-magnification scanning electron microscopy picture of one of the nine electropolished copper samples.

C) Effect of residual oxygen

Figure S7 reveals the surface of several copper specimens after annealing in argon, and after annealing in argon followed by reduction in hydrogen (*i.e.* the morphology of the copper foil just before graphene growth), illustrating the high morphological heterogeneity. Indeed, copper nanoparticles can appear during the CVD process (before the graphene synthesis) owing to the pre-growth annealing under argon (and residual oxidizing gas impurities), after reduction in hydrogen.[6,7] Defected zones such as rolling striations or scratches are more specifically susceptible to oxidation, as we can see in Figure S2d, where white particles are seen all along the striations. Figure S2d clearly displays that these particles are the source of unwanted FLG nucleation. The lack of control over the amount of residual gaseous oxidizing impurities in the reactor of our vacuum-free setup between each CVD procedure is thus a likely additional source of variability. Since EP is supposed to remove any contaminants from the surface of the copper sample, the formation of this copper nanoparticles is a plausible hypothesis to explain the nucleation of FLG adlayers (without considering the nanoparticles segregated from the depth of the copper substrate).

To further investigate the impact of the quantity of residual oxidizing impurities on the final result, we reduce the amount of argon supply during the synthesis (150 or 300 sccm during all the process, instead of 2000 sccm for 15 min then 500 sccm for the remainder of the process, all other conditions being standard). In this way, the atmospheric air contained in the reactor (left open between two CVD syntheses) is less diluted when mixed with argon during the purge step, augmenting the partial pressures in unwanted oxidizing species such as oxygen and water. As seen in Figure S8, large patches of FLG spotted with thicker, much smaller FLG flakes appear as the argon flow drops.

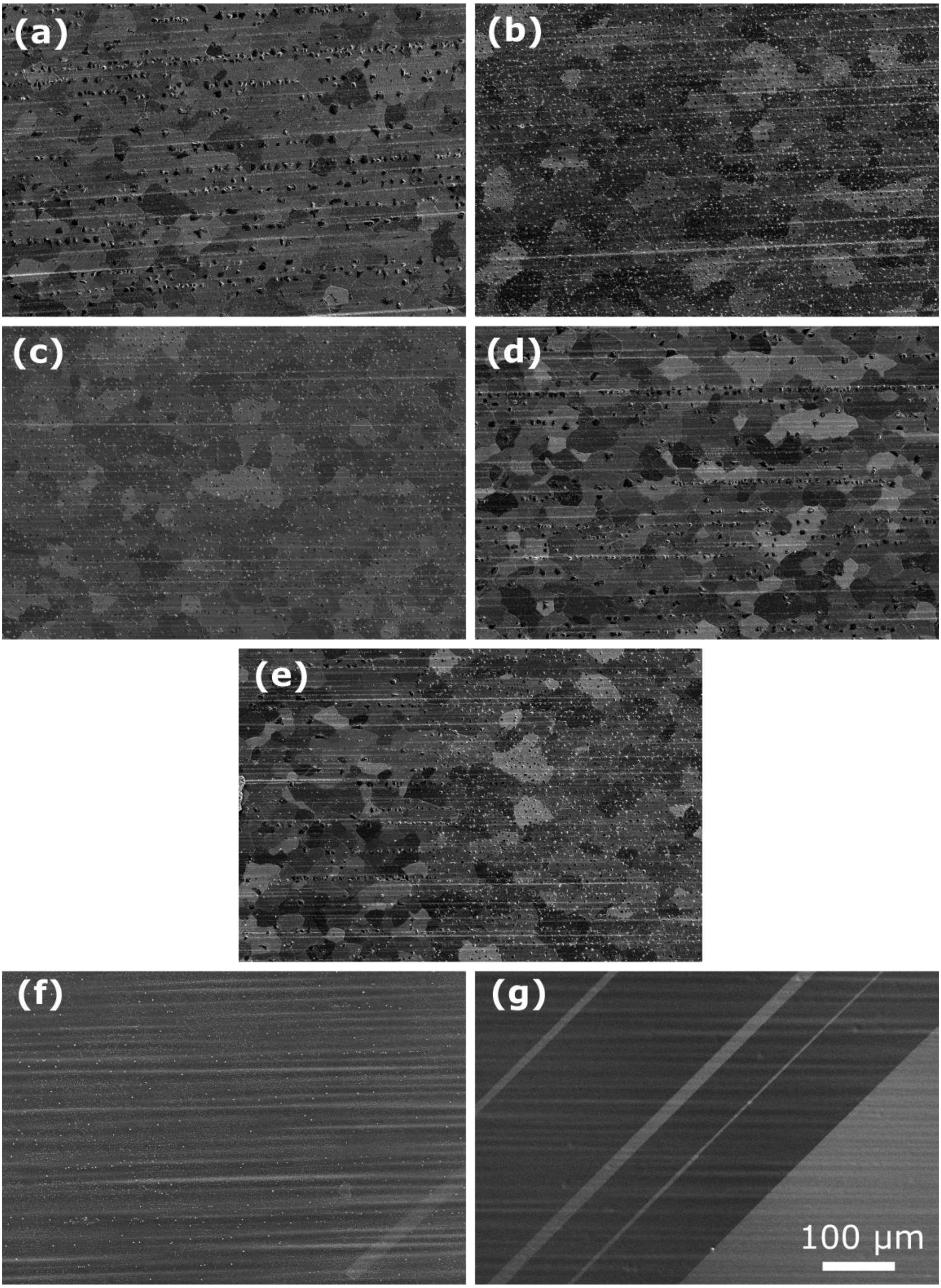

Figure S7: Higher magnification scanning electron microscopy pictures of five samples just after the 15 min oxidation under argon alone (a)-(e) and two additional samples just after oxidation (15 min) and reduction (45 min) (f),(g). The scale bar is identical for all the images.

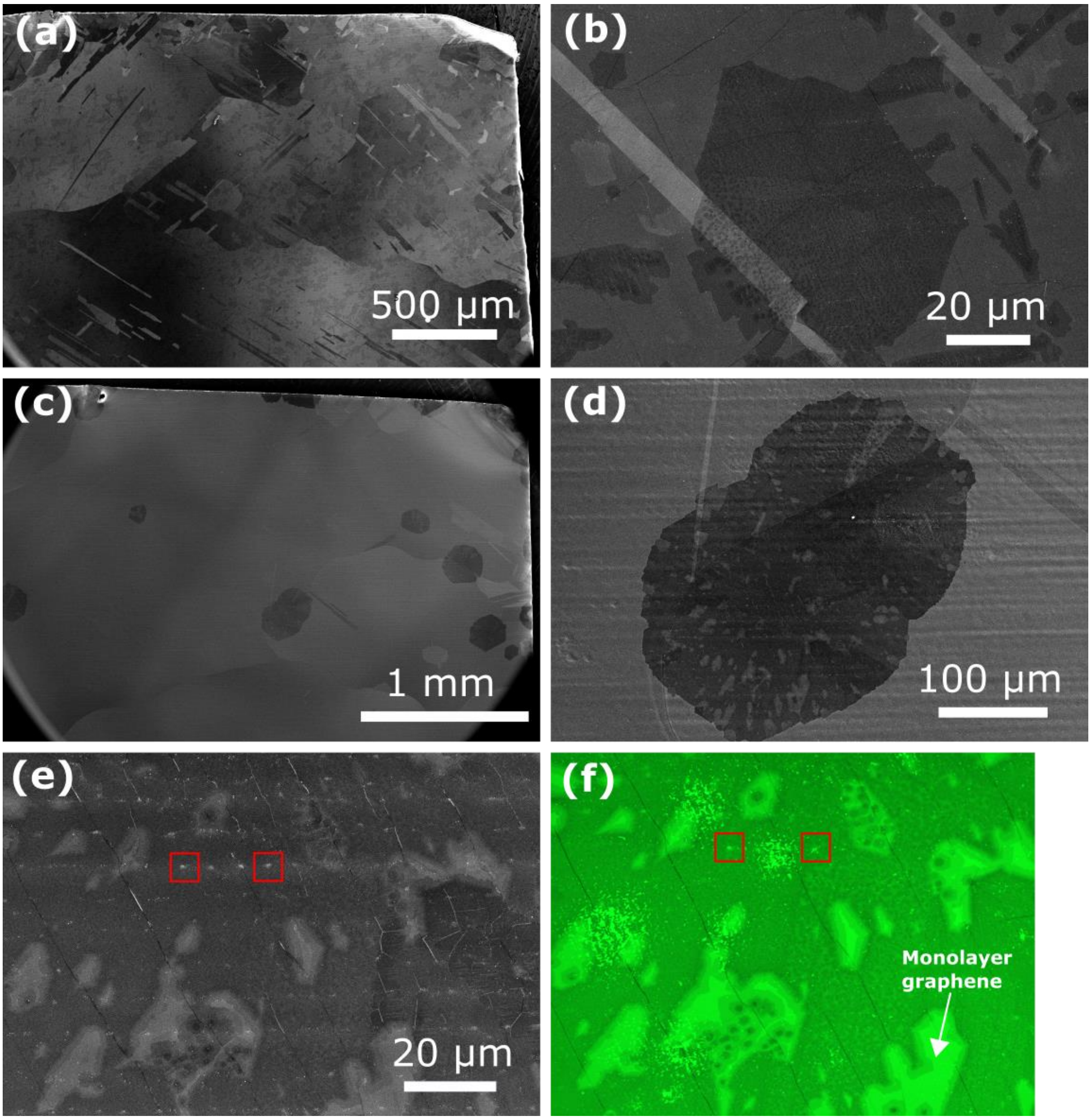

Figure S8: Scanning electron microscopy images of two graphene/copper samples grown under the standard conditions, except for the argon flow, which is decreased to 300 (a),(b) or 150 sccm (c)-(e), respectively. This argon flow drop has the effect of increasing the partial pressure in oxidizing impurities in the reactor, with the consequence of a strong increase in few-layer graphene areas. (f) Optical microscopy image (with a green filter to increase the graphene layer number contrast) of the same area as in panel (e) after transfer onto a 300-nm-thick silicon dioxide piece. Incidentally, another adverse side effect of the presence of contamination on the copper foil before graphene growth is that they are transferred with graphene on the target substrate as seen in the red rectangles (not to mention the impurities introduced by the transfer procedure itself).

D) Growth on a copper foil stacked over a nickel foil

Our previous results plainly emphasize that none of the chemical and electrochemical treatments we have tried result in complete reproducibility. We then attempt to hinder the FLG nucleation by using a Ni foil, serving as a C sink, to support the Cu substrates.[30,31] As seen in Figure S5e, this trial has failed, possibly because the Cu and Ni foils are not perfectly flat and in intimate contact with each other, leaving gaps for methane (CH_4) to diffuse through Cu. Another group has used a W foil inside a Cu enclosure for the same purpose.[32]

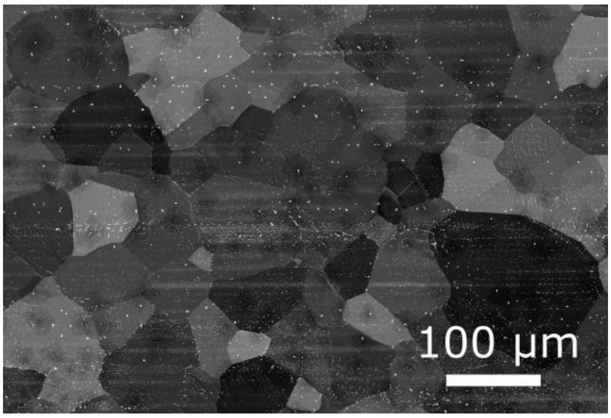

Figure S9: Graphene growth (under the standard conditions) with the copper sample lying over a nickel foil, after glacial acetic acid and deionized water pre-growth treatment.

2) Raman spectroscopy and optical contrast characterization of the samples

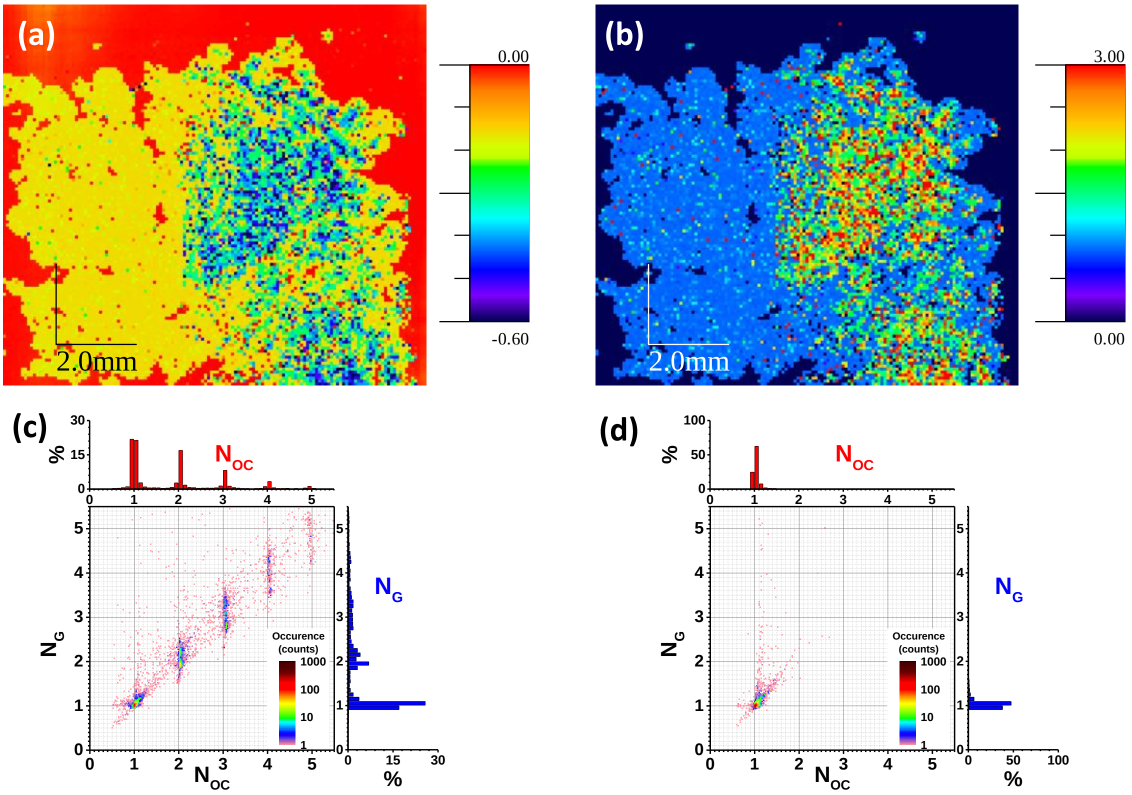

Figure S10: (a) Optical contrast and (b) A_G^{norm} maps (≈1×1 cm² with a 70 µm *xy*-step) of the sample shown in Figure 1c (dilute methane flow of 0.6 sccm during 1 h). (c) and (d) 3D bivariate histogram (0.025 bin size) of N_{OC} and N_G derived from maps (a) and (b) using the expressions 3 and 4 from Ref. [33] (displayed at the end of this section). (c) corresponds to the full map while, for (d), only the left half of the sample is considered. The number of occurrences (frequency counts) is color-coded as shown on the plots. On top (resp. right hand side) are displayed the corresponding histograms of N_{OC} (resp. N_G).

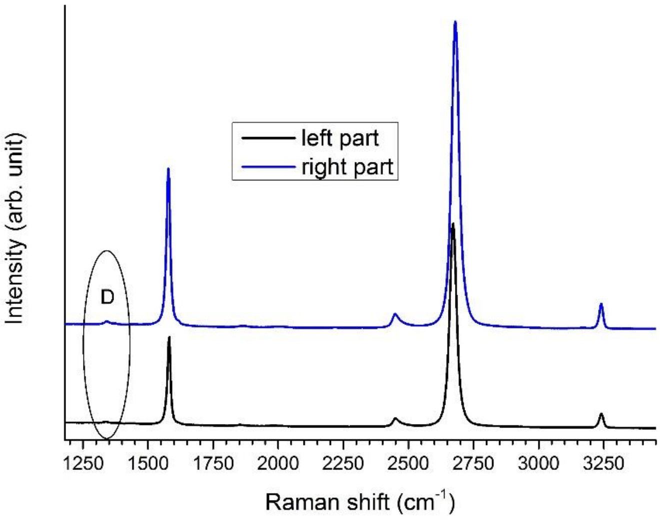

Figure S11: Average Raman spectrum of the left and right part of the sample shown in Figure 1c (dilute methane flow of 0.6 sccm during 1 h).

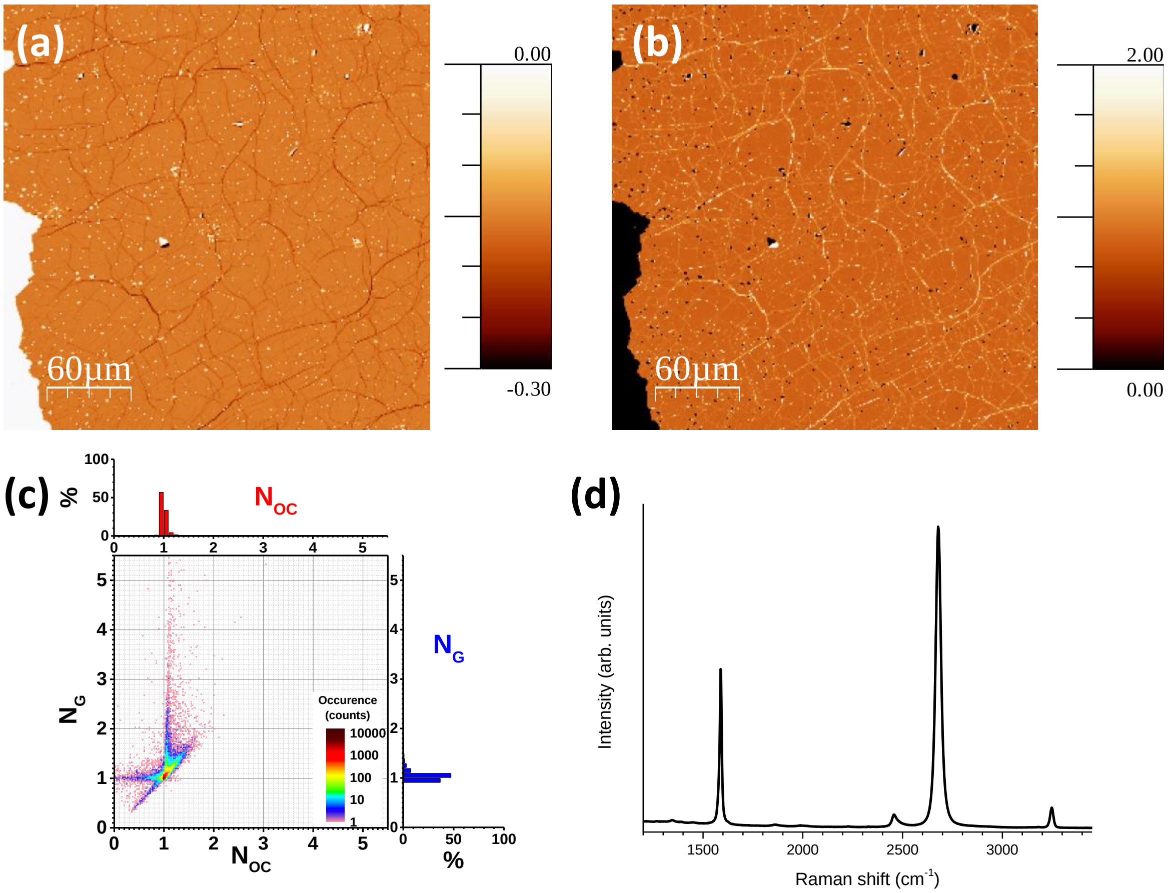

Figure S12: (a) Optical contrast and (b) A_G^{norm} maps (300×300 µm² with a 1 µm *xy*-step) of the sample shown in Figure 1c (dilute methane flow of 0.6 sccm during 1 h). (c) 3D bivariate histogram (0.025 bin size) of N_{OC} and N_{G} derived from maps (a) and (b) using the expressions 3 and 4 from Ref. [33] (displayed at the end of this section). (d) Average Raman spectrum corresponding to the map displayed in (b).

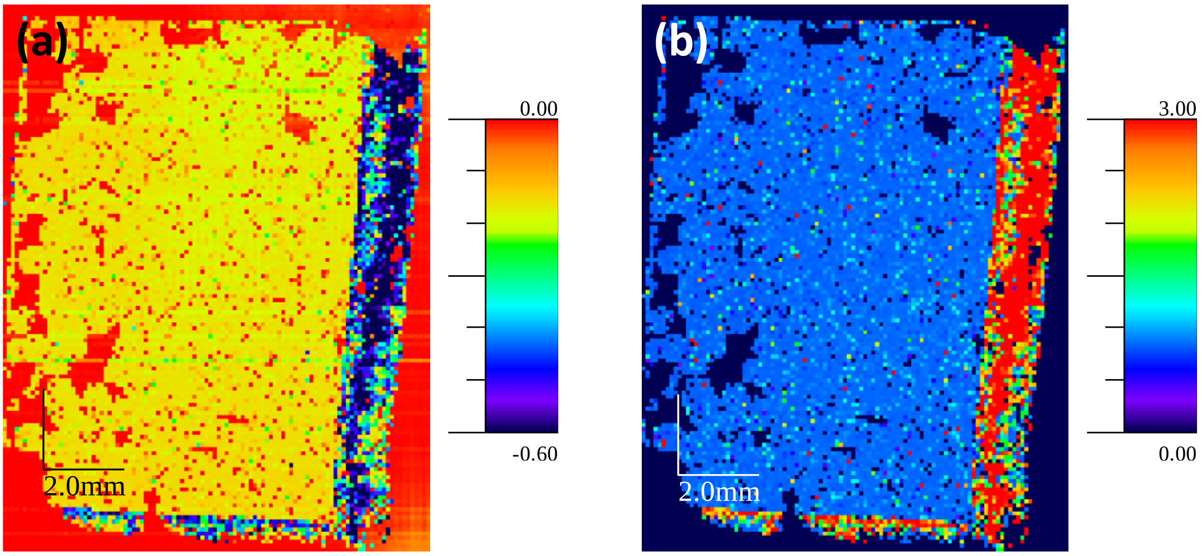

Figure S13: (a) Optical contrast and (b) A_G^{norm} maps (≈1.05×1.35 cm² with a 100 µm *xy*-step) of the sample shown in Figure 2 (dilute methane flow of 1.2 sccm during 1 h).

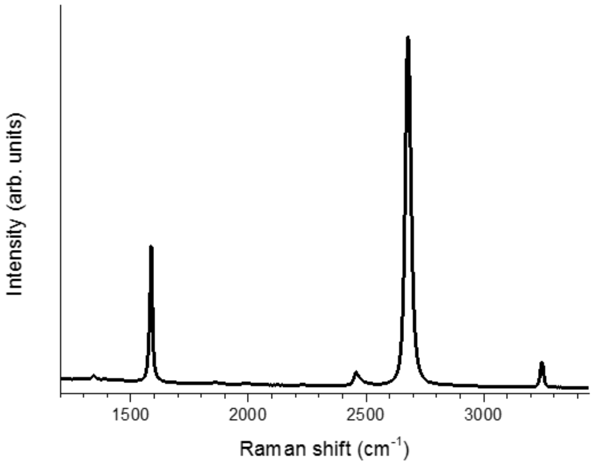

Figure S14: Average Raman spectrum of the sample shown in Figure 2 (dilute methane flow of 1.2 sccm during 1 h), corresponding to the region delimited by the dashed rectangle.

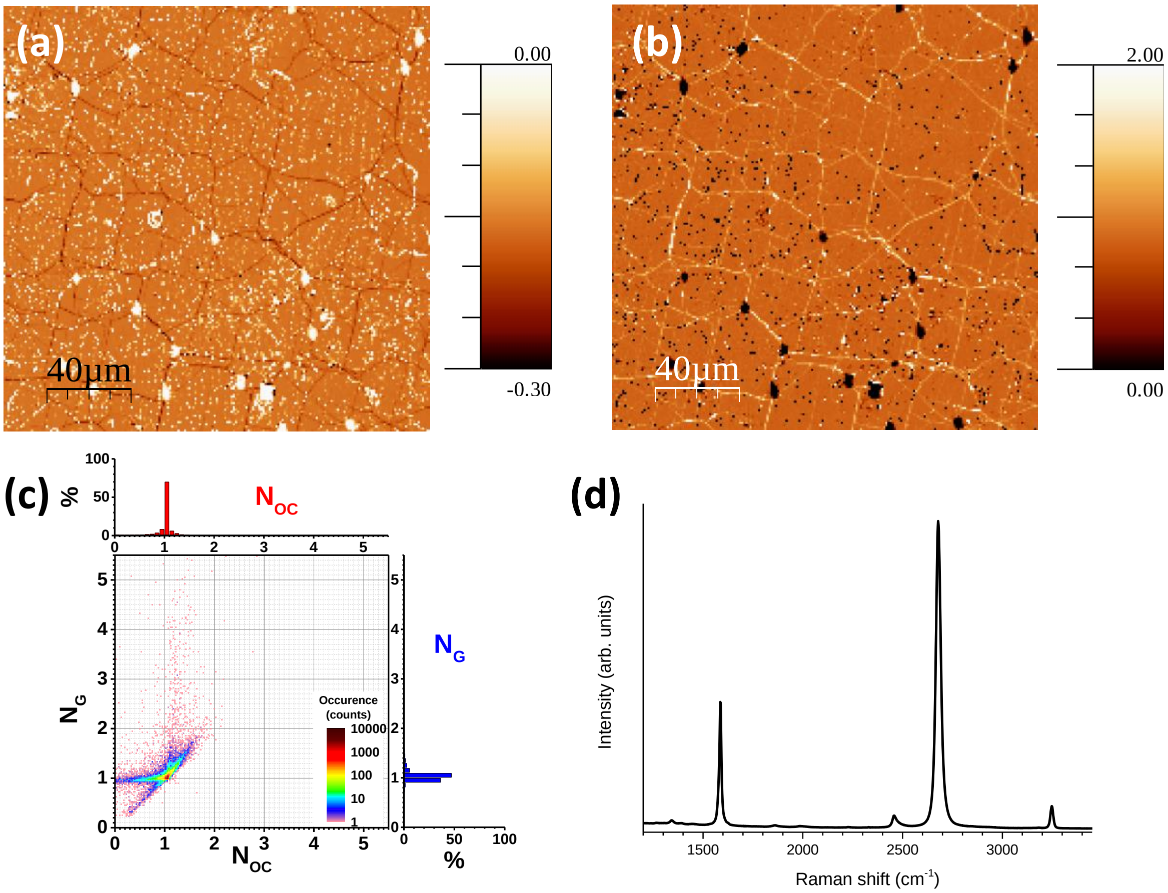

Figure S15: (a) Optical contrast and (b) $A_{\mathrm{G}}^{\mathrm{norm}}$ maps (200×200 µm² with a 1 µm *xy*-step) of the sample shown in Figure 2 (dilute methane flow of 1.2 sccm during 1 h). (c) 3D bivariate histogram (0.025 bin size) of N_{OC} and N_{G} derived from maps (a) and (b) using the expressions 3 and 4 from Ref. [33] (displayed at the end of this section). (d) Average Raman spectrum corresponding to the map displayed in (b).

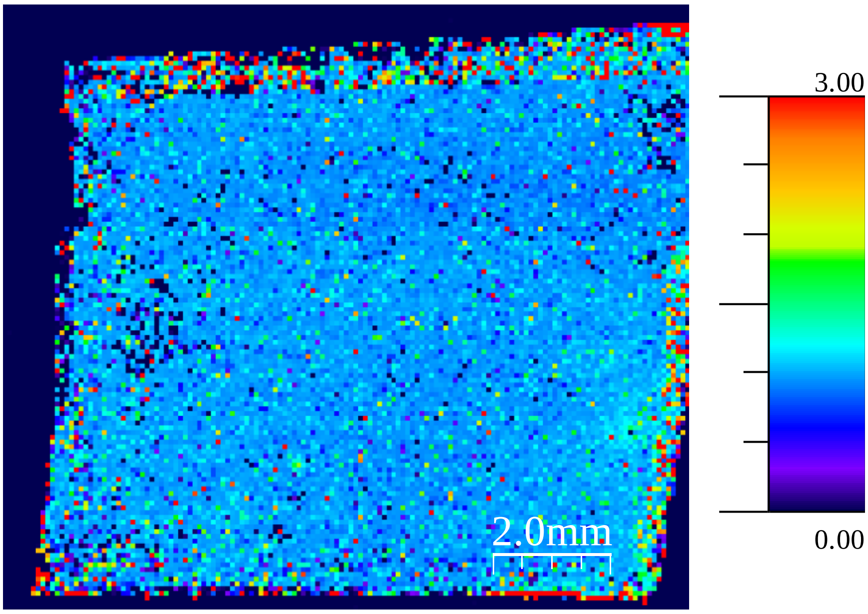

Figure S16: N_G maps (≈1×1.15 cm^2 with a 80 µm *xy*-step) of the sample grown with a dilute methane flow of 3 sccm during 5 min, derived from A_G^{norm} (not shown) using the expression 3 from Ref. [33] (expression (1) given at the end of this section).

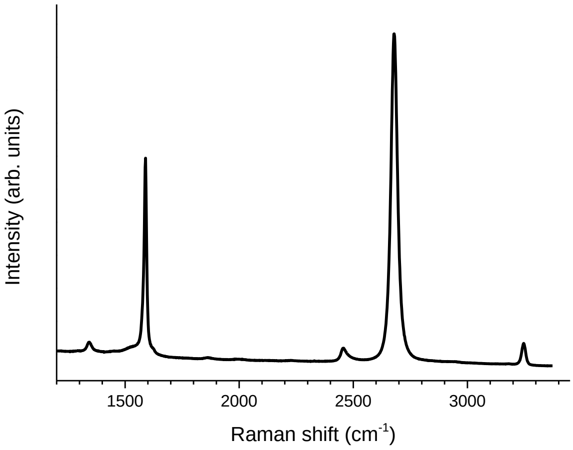

Figure S17: Average Raman spectrum of the sample grown with a dilute methane flow of 3 sccm during 5 min corresponding to the map of Figure S16.

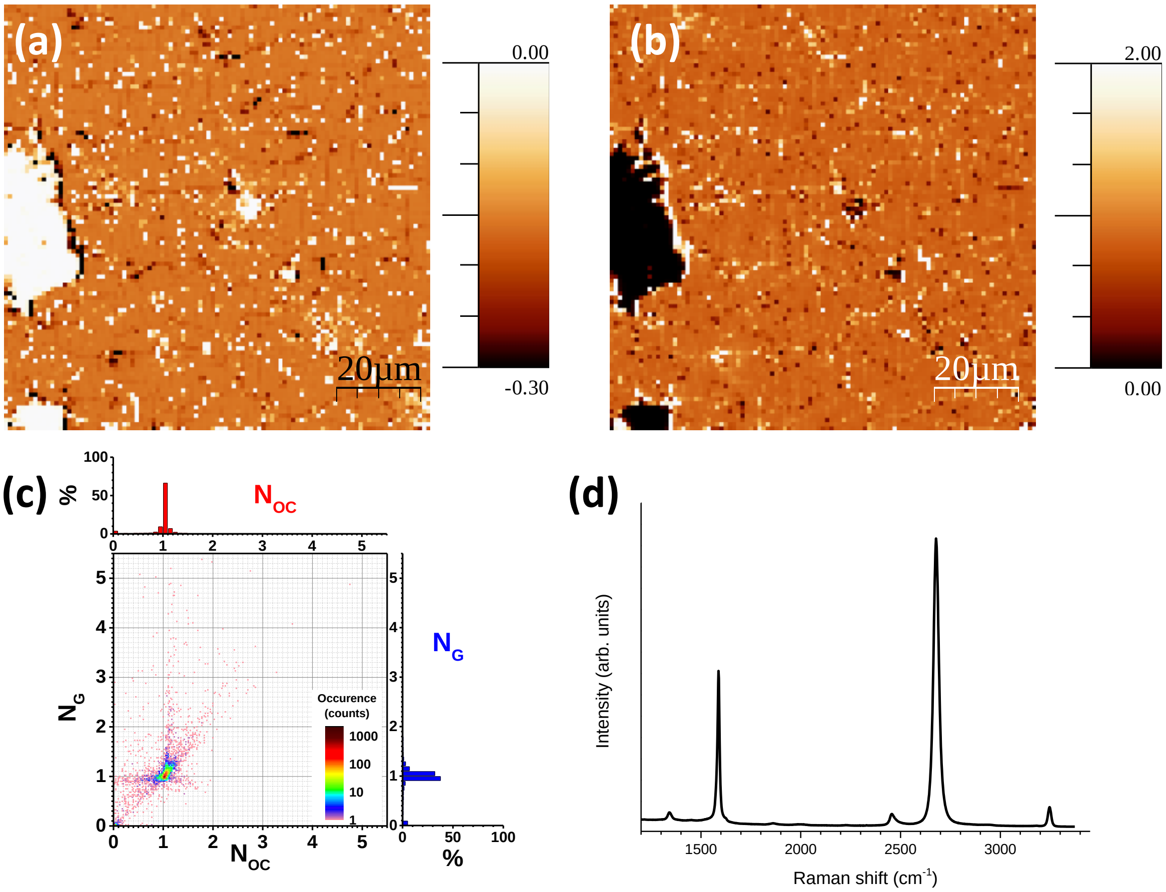

Figure S18: (a) Optical contrast and (b) $A_{\mathrm{G}}^{\mathrm{norm}}$ maps (100×100 µm² with a 1 µm *xy*-step) of the sample grown with a dilute methane flow of 3 sccm during 5 min. (c) 3D bivariate histogram (0.025 bin size) of N_{OC} and N_{G} derived from maps (a) and (b) using the expressions 3 and 4 from Ref. [33] (displayed at the end of this section). (d) Average Raman spectrum corresponding to the map displayed in (b).

Expressions used to calculate the estimated numbers of layers N_{G} and N_{OC}

N_{G} and N_{OC} (the number of layers estimated from $A_{\mathrm{G}}^{\mathrm{Norm}}$ and from the optical contrast (OC), respectively) are obtained using the relations found in Ref. [33]:

$$N_{\mathrm{G}} = 1.05\times A_{\mathrm{G}}^{\mathrm{Norm}} + 0.16\times\left(A_{\mathrm{G}}^{\mathrm{Norm}}\right)^2 \qquad (1)$$

and

$$N_{\mathrm{OC}} = -5.74\times \mathrm{OC} + 4.61\times \mathrm{OC}^2. \qquad (2)$$

3) Electrical characterization

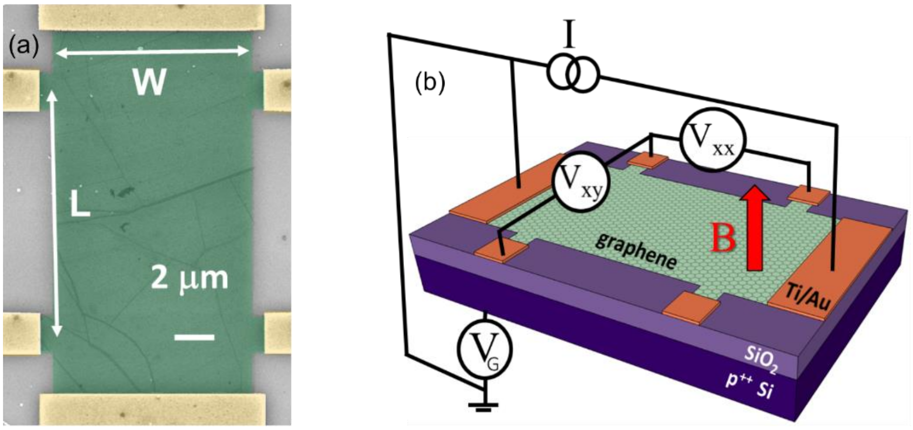

Figure S19: (a) False-colored scanning electron micrograph of a graphene field-effect transistor, with single-layer graphene (green) contacted by Ti/Au electrodes (yellow). (b) Schematic overview of the circuit for field-effect measurements. A current bias of 10 µA is applied to the sample, while the longitudinal voltage V_xx and transversal (Hall) voltage V_xy are measured as a function of the gate voltage V_G and of the magnetic field B, applied perpendicular to the graphene plane.

4) Additional experimental details

Scanning electron microscopy/Energy-dispersive X-ray spectroscopy

The morphology and the size of the Cu grains and graphene domains are monitored with two different microscopes: a Jeol JSM-6010LV InTouchScope at low magnification (operated at an accelerating voltage of 5 kV and a spot size between 30 and 50, with a working distance of 25 mm to increase the field of view, in secondary electron mode) and a Jeol JSM-7500F at high resolution (operated at an accelerating voltage of 1 kV and an emission current of 5 µA, with a working distance of 3 mm, in secondary electron mode with a low gentle beam of 0.2 kV applied to the specimen). Energy-dispersive X-ray spectroscopy mapping is performed with the Jeol JSM-7500F at 15 kV with a probe current of 1 nA and a resolution of 512×384 px.

X-ray photoelectron spectroscopy

Two different spectrometers are used: a K-alpha and an Escalab250Xi from ThermoFischer Scientific. The spectra are recorded at constant pass energy (150 eV for survey; 30 eV for high-resolution spectra; 50 eV for depth profiling). A flood gun (low energy electrons and Ar^+ ions) is used during all the measurements. During the sputtering, the Ar^+ ion gun is operated at an accelerating voltage of 2 kV, with an erosion step of 100 s per cycle. The X-ray photoelectron spectroscopy data are treated with the Avantage software. High-resolution spectra are fitted by Gaussian-Lorentzian lineshapes with an Avantage "smart" background (*i.e.* a Shirley background in most cases, or a linear background in case the lineshape decreases with increasing binding energy). The diameter of the analyzed surface is 250 µm for the surface analysis and 400 µm for the depth profile.

Raman spectroscopy setup

Raman spectra are recorded using an Acton SP2500 spectrometer fitted with a Pylon CCD detector and a grating that enables the measurement of the full spectrum in the 1000–3000 cm^{-1} range within a single acquisition (*i.e.* for a 532 nm laser, 600 grooves/mm grating corresponding to ~2 cm^{-1} between each CCD pixel). The samples are excited with a 532 nm (2.33 eV) laser (Millennia Prime, Newport) through a 100× objective (Numerical Aperture 0.9) and 1 mW impinging on the sample. Optimized focus conditions are checked for each measurement. The samples are mounted on a three-axis piezoelectric stage (Physik Instrumente, 300 µm ranges in xyz) to ensure the precise positioning and focusing of the laser spot and a two-axis piezoelectric stage (Physik Instrumente, 25 mm ranges in xy) for large maps (*i.e.* larger than 300 µm). The laser power is continuously measured by a calibrated photodiode put behind the beam splitter which enables to correct the laser power fluctuations during the sample mapping. To perform simultaneously microreflection (OC) measurements and Raman spectroscopy, a low noise photodiode is placed on the path of the laser beam reflected by the edge filter located in front of the spectrometer's entrance slit. The laser OC, defined by $OC = (R - Rs)/Rs$, where R (resp.

Rs) is the reflected intensity of the 532 nm laser light measured at each point of the sample (resp. on the bare substrate). The whole experimental setup (spectrometer, piezoelectric stage, photodiodes…) is controlled by a dedicated, home-made Labview application. Graphite is used as the Raman intensity reference. To ensure reproducibility, (i) high-quality graphite samples must be used such as HOPG grade ZYA or SCG, (ii) the D-band must be absent from the measured reference spectrum, (iii) optimized focus conditions must be used and (iv) accurate laser incident power and acquisition time normalizations must be performed. The experimental setup is fully enclosed to avoid any external perturbations. Together with its designed great mechanical and laser pointing stabilities, this allows to almost cancel any xyz drifts typically due to ambient temperature changes. A home-made data analysis software is used to treat the data set (including normalization of the intensity with regards to that of HOPG, corrections of the laser fluctuations, background subtraction, fitting of the bands, etc.).

X-ray diffraction

The crystallographic structure of the samples, fixed to silicon substrates to make them flat, has been analyzed by means of an X'Pert PRO Panalytical apparatus using the CuKα radiation (1.54056 Å).

Hall bar fabrication

Devices are fabricated after the CVD graphene is transferred onto a 7×7 mm^2 SiO_2 (300 nm)/p^{++} Si substrate in a wet transfer procedure. A double layer resist mask (PMMA/MA and PMMA 950K) is fabricated using a customized electron beam lithography platform from Raith GmbH to define the contact structures, which are metallized with a titanium adhesion layer (5 nm) and gold (30 nm) contacts using a molecular beam epitaxy system at evaporation rates of ~ 0.1 nm/s and 0.02 nm/s, respectively. Afterwards, a second resist mask (single layer PMMA 950K) is employed as an etch mask in order to define the graphene transport channel using reactive ion etching (channel of width W = 10 µm and length L = 12 µm). Each of these two lithography steps is followed by lift-off in acetone.

Transport measurements

Electronic transport measurements are carried out in an Oxford Instruments He Heliox cryostat with a base temperature of 300 mK and a 5 T magnet. Current bias and gate voltage are applied using a Keithley model 2612 dual channel source meter, while transversal and longitudinal voltage are probed using a Hewlett-Packard 34420A nanovolt meter. The vacuum chamber containing sample is evacuated down to ~5×10^{-6} mbar.

---

[1] Zhang, B.; Lee, W. H.; Piner, R.; Kholmanov, I.; Wu, Y.; Li, H.; Ji, H.; Ruoff, R. S. Low-Temperature Chemical Vapor Deposition Growth of Graphene from Toluene on Electropolished Copper Foils. *ACS Nano* **2012**, *6*, 2471–2476.

[2] Murdock, A. T.; Koos, A.; Britton, T. B.; Houben, L.; Batten, T.; Zhang, T.; Wilkinson, A. J.; Dunin-Borkowski, R. E.; Lekka, C. E.; Grobert, N. Controlling the Orientation, Edge Geometry, and Thickness of Chemical Vapor Deposition Graphene. *ACS Nano* **2013**, *7*, 1351–1359.

[3] Chen, S.; Ji, H.; Chou, H.; Li, Q.; Li, H.; Suk, J. W.; Piner, R.; Liao, L.; Cai, W.; Ruoff, R. S. Millimeter-Size Single-Crystal Graphene by Suppressing Evaporative Loss of Cu During Low Pressure Chemical Vapor Deposition. *Adv. Mater.* **2013**, *25*, 2062–2065.

[4] Han, G. H.; Güneş, F.; Bae, J. J.; Kim, E. S.; Chae, S. J.; Shin, H.-J.; Choi, J.-Y.; Pribat, D.; Lee, Y. H. Influence of Copper Morphology in Forming Nucleation Seeds for Graphene Growth. *Nano Lett.* **2011**, *11*, 4144–4148.

[5] Ibrahim, A.; Akhtar, S.; Atieh, M.; Karnik, R.; Laoui, T. Effects of Annealing on Copper Substrate Surface Morphology and Graphene Growth by Chemical Vapor Deposition. *Carbon* **2015**, *94*, 369–377.

[6] Gan, L.; Luo, Z. Turning off Hydrogen To Realize Seeded Growth of Subcentimeter Single-Crystal Graphene Grains on Copper. *ACS Nano* **2013**, *7*, 9480–9488.

[7] Reckinger, N.; Tang, X.; Joucken, F.; Lajaunie, L.; Arenal, R.; Dubois, E.; Hackens, B.; Henrard, L.; Colomer, J.-F. Oxidation-Assisted Graphene Heteroepitaxy on Copper Foil. *Nanoscale* **2016**, *8*, 18751–18759.

[8] Suzuki, S.; Nagamori, T.; Matsuoka, Y.; Yoshimura, M. Threefold Atmospheric-Pressure Annealing for Suppressing Graphene Nucleation on Copper in Chemical Vapor Deposition. *Jpn. J. Appl. Phys* **2014**, *53*, 095101.

[9] Wang, Z.-J.; Weinberg, G.; Zhang, Q.; Lunkenbein, T.; Klein-Hoffmann, A.; Kurnatowska, M.; Plodinec, M.; Li, Q.; Chi, L.; Schloegl, R.; et al. Direct Observation of Graphene Growth and Associated Copper Substrate Dynamics by in Situ Scanning Electron Microscopy. *ACS Nano* **2015**, *9*, 1506–1519.

[10] Murdock, A. T.; van Engers, C. D.; Britton, J.; Babenko, V.; Meysami, S. S.; Bishop, H.; Crossley, A.; Koos, A. A.; Grobert, N. Targeted Removal of Copper Foil Surface Impurities for Improved Synthesis of CVD Graphene. *Carbon* **2017**, *122*, 207–216.

[11] Kim, S. M.; Hsu, A.; Lee, Y.-H.; Dresselhaus, M.; Palacios, T.; Kim, K. K.; Kong, J. The Effect of Copper Pre-Cleaning on Graphene Synthesis. *Nanotechnol.* **2013**, *24*, 365602.

[12] Fan, L.; Wang, K.; Wei, J.; Zhong, M.; Wu, D.; Zhu, H. Correlation between Nanoparticle Location and Graphene Nucleation in Chemical Vapour Deposition of Graphene. *J. Mater. Chem. A* **2014**, *2*, 13123–13128.

[13] Jacobberger, R. M.; Arnold, M. S. Graphene Growth Dynamics on Epitaxial Copper Thin Films. *Chem. Mater.* **2013**, *25*, 871–877.

[14] Jung, D. H.; Kang, C.; Kim, M.; Cheong, H.; Lee, H.; Lee, J. S. Effects of Hydrogen Partial Pressure in the Annealing Process on Graphene Growth. *J. Phys. Chem. C* **2014**, *118*, 3574–3580.

[15] Lisi, N.; Dikonimos, T.; Buonocore, F.; Pittori, M.; Mazzaro, R.; Rizzoli, R.; Marras, S.; Capasso, A. Contamination-Free Graphene by Chemical Vapor Deposition in Quartz Furnaces. *Sci. Rep.* **2017**, *7*, 9927.

[16] Zhang, Y.; Li, Z.; Kim, P.; Zhang, L.; Zhou, C. Anisotropic Hydrogen Etching of Chemical Vapor Deposited Graphene. *ACS Nano* **2012**, *6*, 126–132.

[17] Shivayogimath, A.; Mackenzie, D.; Luo, B.; Hansen, O.; Bøggild, P.; Booth, T. J. Probing the Gas-Phase Dynamics of Graphene Chemical Vapour Deposition Using in-Situ UV Absorption Spectroscopy. *Sci. Rep.* **2017**, *7*, 6183.

---

[18] Vlassiouk, I.; Regmi, M.; Fulvio, P.; Dai, S.; Datskos, P.; Eres, G.; Smirnov, S. Role of Hydrogen in Chemical Vapor Deposition Growth of Large Single-Crystal Graphene. *ACS Nano* **2011**, *5*, 6069–6076.

[19] Hao, Y.; Bharathi, M. S.; Wang, L.; Liu, Y.; Chen, H.; Nie, S.; Wang, X.; Chou, H.; Tan, C.; Fallahazad, B.; et al. The Role of Surface Oxygen in the Growth of Large Single-Crystal Graphene on Copper. *Science* **2013**, *342*, 720–723.

[20] Luo, Z.; Lu, Y.; Singer, D. W.; Berck, M. E.; Somers, L. A.; Goldsmith, B. R.; Johnson, A. T. C. Effect of Substrate Roughness and Feedstock Concentration on Growth of Wafer-Scale Graphene at Atmospheric Pressure. *Chem. Mater.* **2011**, *23*, 1441–1447.

[21] Wang, H.; Wang, G.; Bao, P.; Yang, S.; Zhu, W.; Xie, X.; Zhang, W.-J. Controllable Synthesis of Submillimeter Single-Crystal Monolayer Graphene Domains on Copper Foils by Suppressing Nucleation. *J. Am. Chem. Soc.* **2012**, *134*, 3627–3630.

[22] Howsare, C. A.; Weng, X.; Bojan, V.; Snyder, D.; Robinson, J. A. Substrate Considerations for Graphene Synthesis on Thin Copper Films. *Nanotechnol.* **2012**, *23*, 135601.

[23] Kim, H.; Song, I.; Park, C.; Son, M.; Hong, M.; Kim, Y.; Kim, J. S.; Shin, H.-J.; Baik, J.; Choi, H. C. Copper-Vapor-Assisted Chemical Vapor Deposition for High-Quality and Metal-Free Single-Layer Graphene on Amorphous SiO_2 Substrate. *ACS Nano* **2013**, *7*, 6575–6582.

[24] Orofeo, C. M.; Hibino, H.; Kawahara, K.; Ogawa, Y.; Tsuji, M.; Ikeda, K.; Mizuno, S.; Ago, H. Influence of Cu Metal on the Domain Structure and Carrier Mobility in Single-Layer Graphene. *Carbon* **2012**, *50*, 2189–2196.

[25] Wu, W.; Jauregui, L. A.; Su, Z.; Liu, Z.; Bao, J.; Chen, Y. P.; Yu, Q. Growth of Single Crystal Graphene Arrays by Locally Controlling Nucleation on Polycrystalline Cu Using Chemical Vapor Deposition. *Adv. Mater.* **2011**, *23*, 4898–4903.

[26] Liu, L.; Zhou, H.; Cheng, R.; Yu, W. J.; Liu, Y.; Chen, Y.; Shaw, J.; Zhong, X.; Huang, Y.; Duan, X. High-Yield Chemical Vapor Deposition Growth of High-Quality Large-Area AB-Stacked Bilayer Graphene. *ACS Nano* **2012**, *6*, 8241–8249.

[27] Zhou, H.; Yu, W. J.; Liu, L.; Cheng, R.; Chen, Y.; Huang, X.; Liu, Y.; Wang, Y.; Huang, Y.; Duan, X. Chemical Vapour Deposition Growth of Large Single Crystals of Monolayer and Bilayer Graphene. *Nat. Commun.* **2013**, *4*, 2096.

[28] Chavez, K. L.; Hess, D. W. A Novel Method of Etching Copper Oxide Using Acetic Acid. *J. Electrochem. Soc.* **2001**, *148*, G640.

[29] Yu, H. K.; Balasubramanian, K.; Kim, K.; Lee, J.-L.; Maiti, M.; Ropers, C.; Krieg, J.; Kern, K.; Wodtke, A. M. Chemical Vapor Deposition of Graphene on a “Peeled-Off” Epitaxial Cu(111) Foil: A Simple Approach to Improved Properties. *ACS Nano* **2014**, *8*, 8636–8643.

[30] Ding, D.; Solís-Fernández, P.; Hibino, H.; Ago, H. Spatially Controlled Nucleation of Single-Crystal Graphene on Cu Assisted by Stacked Ni. *ACS Nano* **2016**, *10*, 11196–11204.

[31] Abidi, I. H.; Liu, Y.; Pan, J.; Tyagi, A.; Zhuang, M.; Zhang, Q.; Cagang, A. A.; Weng, L.-T.; Sheng, P.; Goddard, W. A.; et al. Regulating Top-Surface Multilayer/Single-Crystal Graphene Growth by “Gettering” Carbon Diffusion at Backside of the Copper Foil. Adv. Funct. Mater. 2017, 27, 1700121.

[32] Fang, W.; Hsu, A.; Shin, Y. C.; Liao, A.; Huang, S.; Song, Y.; Ling, X.; Dresselhaus, M. S.; Palacios, T.; Kong, J. Application of Tungsten as a Carbon Sink for Synthesis of Large-Domain Uniform Monolayer Graphene Free of Bilayers/Multilayers. Nanoscale 2015, 7, 4929–4934.

[33] Bayle, M.; Reckinger, N.; Felten, A.; Landois, P.; Lancry, O.; Dutertre, B.; Colomer, J.-F.; Zahab, A.-A.; Henrard, L.; Sauvajol; et al. Determining the number of layers in few-layer graphene by combining Raman spectroscopy and optical contrast. *J. Raman Spectrosc.* **2018**, *49*, 36–45.